PAPER • OPEN ACCESS

1D modeling of plasma streamers at ammonia-air flame conditions

View the article online for updates and enhancements.

1D modeling of plasma streamers at ammonia-air flame conditions

Taaresh Sanjeev Taneja[1] ⬥**, Hariswaran Sitaraman**[2]⬥ **and Suo Yang**[1,*] ⬥

[1] Department of Mechanical Engineering, University of Minnesota—Twin Cities, 111 Church St SE, Minneapolis, MN 55455, United States of America
[2] Computational Science Center, National Renewable Energy Laboratory, 15013 Denver W Pkwy, Golden, CO 80401, United States of America

E-mail: suo-yang@umn.edu, tanej013@umn.edu and hariswaran.sitaraman@nrel.gov

CrossMark

Abstract

Self-consistent 1D modeling of streamers in ammonia-oxygen-nitrogen-water mixtures has been performed in this work. A fluid model that includes species transport, electrostatic potential, and detailed chemistry was developed and verified. This model is then used to simulate the avalanche, streamer formation and propagation phases, driven by a nanosecond voltage pulse, at different thermochemical conditions derived from a 1D laminar premixed ammonia-air flame. The applicability of the Meek's criterion in predicting the streamer inception location was successfully confirmed. Streamer formation and propagation duration were found to vary significantly with different thermochemical conditions, due to the difference in ionization rates. The thermochemical state also affected the breakdown characteristics which was tested by maintaining the background reduced electric field constant. Detailed kinetic analyses revealed the importance of $O(^1D)$ in the production of key radicals, such as O, OH, and NH_2. Furthermore, the contributions of the dissociative electronic excitation of NH_3 towards the production of H and NH_2 radicals have also been reported. Spatial and temporal evolution of the electron energy loss fractions for various inelastic collision processes at different thermochemical states uncovered the input plasma energy spent of fuel dissociation and the large variability in the dominant processes during the avalanche and streamer propagation phases. The methodology and analyses reported in this work are key towards developing effective strategies for controlled nanosecond-pulsed non-equilibrium plasma sources used for ammonia ignition and flame stabilization.

Supplementary material for this article is available online

---

* Author to whom any correspondence should be addressed.

J. Phys. D: Appl. Phys. **58** (2025) 015204

T S Taneja *et al*

1. Introduction

The field of ammonia combustion has gained wide-spread traction in the past decade given the potential of ammonia to become a carbon-free fuel for transportation and electricity generation applications [1, 2]. Well known challenges of ammonia combustion include low flame speed, high heat of ignition, narrow flammability range, and increased production of NO_x. Non-equilibrium plasma assisted combustion of ammonia is now being explored as a promising technology to address several of these challenges. The work by Choe *et al* [3] was one of the first experimental efforts that showed the positive effects of non-equilibrium plasma on extending the lean blow-off (LBO) limit and the simultaneous reduction of NO_x emission levels of an ammonia-air flame. Lin *et al* [4] showed that the flame speed and the combustion limits of ammonia-air combustion can be enhanced by using a gliding arc plasma reactor with a swirl burner. They also showed that NO can be limited to under 100 ppm in a lean ammonia-air flame, however the exact mechanisms driving these benefits were not discussed in detail. Similarly, Kim *et al* [5] discussed the use of an alternating-current (AC) dielectric barrier discharge (DBD) reactor in their swirl dump combustor to stabilize turbulent NH_3-air flames. They also performed NH_2^* chemiluminescence, which allowed them to postulate that NO reduction pathways are facilitated by NH_2, that is produced in increased amounts by a non-equilibrium plasma. They also observed that increasing the discharge power resulted in lower levels of NO_x emission in lean ammonia flames. Clearly, fundamental investigations focused on the interaction of the plasma discharge with the ammonia-air flame is necessary to understand the mechanisms responsible for these experimental observations. Zhong *et al* [6] conducted comprehensive chemical kinetic analyses for efficient ammonia oxidation using nanosecond DBD discharges. They concluded that an optimal electric field exists, which helps in ammonia dissociation rather than the redirection of electron energy into vibrational excitation of N_2 (at lower than optimal electric field) or dissociation of N_2 (at higher than optimal electric field). Further, they also observed that tuning the discharge frequency allowed for the accumulation of $HO_2/NH_2/NH$ radicals, which eventually help in efficient oxidation and reduced N_2O emissions. Several numerical studies have focused on evaluating the impact of nanosecond pulsed non-equilibrium plasma on reducing the ignition delay [7–13], improving the flame speed [9, 14], extending the lean ignition limit [15], as well as NO_x reduction [8, 11, 12] from ammonia combustion. All these works probe into the detailed kinetic and thermal pathways enabled by the plasma.

Nanosecond pulsed plasma discharges produced in pin-pin, pin-plane, pin-ring, etc configurations are common sources used for plasma assisted ignition and flame stabilization [16–20]. Depending on the applied voltage, electrode geometry and material, and the gas temperature and pressure, the discharge produced can be in the corona, glow, or nanosecond spark regimes [21] (at atmospheric pressures and above). All these regimes typically feature an electron avalanche that transitions to a streamer for $pd \gtrsim 200$ Torr-cm (where p is the gas pressure and d is the inter-electrode distance), and when the applied electric field is greater than the breakdown field of a particular gas. Streamers can further propagate and branch depending on the effective ionization coefficient and other background ionization pathways. Depending on the duration of the pulse, the gas composition, temperature, and the inter-electrode gap distance, these streamers can connect the two electrodes, thereby forming a conducting channel, which can further result in enhanced gas heating due to increased current flow during the the spark phase. If the voltage is applied for an even longer duration, equilibration of the gas and electron temperatures can occur, which is referred to as the arc phase. Thus, dynamics, such as avalanche to streamer transition, streamer propagation, streamer to spark transition, and the resultant regime of the plasma, depends strongly on the local thermochemical state, especially in a dynamic combustible environment. The thermochemical state of the gas into which the electrical energy from nanosecond repetitive pulses are deposited can keep changing based on the reactor/combustor geometry, the evolving ignition kernel, the flame condition, and the pulse frequency. Hence, it is important to study the influence of the gas composition, temperature, and total number density on the physics of the plasma discharge. This so called 'backward coupling' (i.e. combustion affecting the plasma discharge) was experimentally investigated by Guerra-Garcia and Pavan [22, 23], where the DBD plasma discharge regime was observed to change from a uniform discharge in the burnt gas products of the transversely passing flame, to a filamentary micro-discharge regime after the flame had quenched and the burnt gas products had cooled.

Numerical investigations have also been performed to assess the effect of gas temperature to sustain a glow discharge regime in air [24]. In Tholin and Bourdon [24], it was found that at 1000 K, the negative and positive streamers connect approximately at the same time as the pulse duration, which prevented transition to the spark phase. Similarly, reduction in the average electric field for achieving streamer connection was observed at higher temperatures in the numerical simulations presented in Aleksandrov and Bazelyan [25]. A comprehensive review on streamers was provided in Nijdam *et al* [26], where the authors described the effects of the electron energy losses, photo-ionization, and attachment rates on the differences in streamer dynamics for varied thermochemical conditions. The effect of gas composition was specifically studied using 3D particle-in-cell (PIC) simulations in Bouwman *et al* [27], where they showed that adding methane to pure air resulted in suppressed photo-ionization which eventually led to streamer branching. However, to the best of our knowledge, no work on modeling streamers in ammonia-air combustible mixtures has been published yet. Preliminary results on this study were shared in our previous conference article [28]. Several improvements in terms of the numerical schemes, verification cases and chemical kinetics analyses have been made

and included in the current article, as compared to our previous conference article [28].

The focus of this paper is on simulating the ionization front propagation dynamics and kinetics at various states of a freely propagating laminar ammonia-air flame using a self-consistent 1D plasma fluid model. While self-consistent 1D models such as the one used in this work cannot capture the curvature induced field enhancements at the streamer head, capture sheaths around curved electrodes or predict stochastic effects of streamer branching due to photoionization and other secondary ionization events, they can nonetheless provide valuable insights on electron energy budgets, avalanche to streamer transition condition [29, 30], and probe into the chemical kinetics associated with the streamer dynamics by providing an accurate enough spatiotemporal variation of all quantities of interest in the inter-electrode gap. Moreover, the less expensive computations compared to 2D / 3D models allows usage of larger chemical mechanisms with 1D streamer modeling. It should also be noted that the configurations modeled in this work do not aim to mimic an experimental setup, but qualitative agreements regarding the pathways for radical production were obtained, with a recently published paper investigating plasma assisted ammonia combustion, as is shown later in this paper.

Most typical combustors in engines and gas turbines that use non-equilibrium pulsed plasma for ignition have gap distances of the order of 2–10 mm [31, 32] to achieve breakdown with a reasonable inter-electrode peak voltage of 5–30 kV. This enables the deposition of a few mJ of energy in 5–100 ns in a small volume to gain high enough power densities to produce high temperature and radical-rich hot-spots. Thus, the inter-electrode gap in this work has been chosen to be 4 mm, which falls in the typical range of inter-electrode gap distances for producing nanosecond pulsed plasma. Moreover, depending on the fuel, flow conditions, pre-ionization levels and the local thermochemistry in the inter-electrode gap, different modes of the discharge may be produced. One of the direct consequences of this work on designing nanosecond repetitively pulsed ignition systems for ammonia-fueled propulsion devices is that streamers form and propagate much faster under different flame conditions, which is important for deciding the pulse energy and duration of each pulse in a developing flame. Furthermore, the applied voltage or the time duration of the pulse cannot be simply scaled based on the total number density at any given instance. The threshold breakdown field and the critical field for streamer propagation varies with the thermochemistry in the region of ignition. Also, understanding the distribution of the input plasma energy into various channels can help to optimize the parameters of the pulsed discharge system to achieve desirable fast gas heating and radical generation effects. These can be design parameters such as the inter-electrode gap distance, electrode geometry, etc or operating parameters such as pulse frequency, energy per pulse, pulse duration, etc. Hence, effective control strategies to minimize the input power requirements for an ignition system can be influenced by understanding the effect of these

parameters on the plasma kinetics and dynamics. The overarching outcome of this work is the detailed analysis of plasma dynamics and kinetics including pathways of radical production and energy loss fractions during avalanche to streamer transition and streamer propagation at ammonia-air flame conditions using a self-consistent 1D model. Such a predictive tool can help control pulsed plasma sources for effective ignition and pave the way for alleviating the challenges of ammonia combustion.

Section 2.1 presents the governing equations and the numerical schemes used to simulate electron avalanches, streamer formation and propagation. Section 2.2 contains comparisons of our 1D plasma fluid solver developed for this work, with existing fluid and particle-in-cell (PIC) simulation results available in the literature. Next, Section 3 presents the results for avalanche-to-streamer transition and streamer propagation using the thermochemical conditions from a 1D laminar ammonia-air flame. The applicability of the Meek's criterion is also investigated in this section. Finally, section 4 highlights the important conclusions of this research.

2. Numerical methodology and solver verification

Convection–diffusion-reaction equations along with Poisson's equation for self-consistent electrostatic potential are solved for modeling nanosecond plasma discharges at atmospheric pressures and beyond in this work, similar to previous works [33, 34]. Section 2.1 contains the governing equations and the numerical schemes used to simulate avalanche-to-streamer transition and streamer propagation. The solver has been verified by comparing the results with two benchmark cases in the literature. These have been described in section 2.2.

2.1. Governing equations and numerical schemes

Species conservation equations (equation (1)) with the drift-diffusion approximation (equation (2)) for the flux term is used to evolve the number densities of all the species in the plasma:

$$\frac{\partial n_k}{\partial t} + \vec{\nabla} \cdot \vec{\Gamma}_k = \dot{\omega}_k, \tag{1}$$

$$\vec{\Gamma}_k = \mu_k n_k \vec{E} - D_k \vec{\nabla}(n_k), \tag{2}$$

where n_k is the number density, Γ_k is the total flux, and $\dot{\omega}_k$ is the net production rate of the kth species. In equation (2), μ_k and D_k are the mobility and mass diffusivity (i.e. diffusion coefficient) of the kth species, and $\vec{E}$ is the electric field. The mobility of all neutral species is zero, and thus the neutral species transport is only due to diffusion. The cases considered in this work do not have any bulk convection. The species production rate contributions via electron impact reactions are evaluated using pre-tabulated rate coefficients obtained from an offline Boltzmann solve with the two term approximation using BOLSIG+ [35]. The detailed list of reactions and the

rate coefficients have been provided as part of the supplementary material.

The evolution of the electric field, $\vec{E}$, is governed by the Poisson's equation for electrostatic potential ϕ:

$$\nabla^2 \phi + \frac{e}{\epsilon_0} \sum_{k=1}^{N_{sp}} Z_k n_k = 0, \tag{3}$$

$$\vec{E} = -\vec{\nabla}\phi. \tag{4}$$

In equation (3), $e = 1.602 \times 10^{-19}$ C is the electronic charge, $\epsilon_0 = 8.854 \times 10^{-12}$ m^{-3}kg^{-1}s^{4}A^2 is the permittivity of free space, N_{sp} is the total number of species including electrons, and Z_k is the charge of the kth species.

Finally, the local mean electron energy density, $E_e = (3/2)n_e k_B T_e$, is computed by solving equation (5):

$$\frac{\partial E_e}{\partial t} + \vec{\nabla} \cdot \vec{\Gamma}_{E_e} = \dot{S}_{E_e}, \tag{5}$$

where $\vec{\Gamma}_{E_e}$ is the flux of the local electron energy density E_e, which is also expressed using a drift-diffusion formulation as follows:

$$\vec{\Gamma}_{E_e} = \mu_\epsilon E_e \vec{E} - D_\epsilon \vec{\nabla}(E_e), \tag{6}$$

where the mobility (μ_ε) and diffusion coefficient (D_ε) for the electron energy ($\epsilon = E_e/n_e$) are obtained as functions of the local mean electron energy E_e from BOLSIG+ [35]. The source term $\dot{S}_{E_e}$ on the right-hand-side (RHS) is given by

$$\dot{S}_{E_e} = -e\vec{\Gamma}_e \cdot \vec{E} - \frac{3}{2} n_e k_B (T_e - T_g) \frac{2m_e}{m_b} \nu - \sum_i \Delta E_i r_i. \tag{7}$$

Here, the first term represents the total electron Joule heating: i.e. the energy gained by the electrons from the resultant electric field. The second term is the electron energy loss due to elastic collisions with gas molecules (which are much heavier than electrons), where T_g is the gas temperature, m_e and m_g are the molecular weights of an electron and the neutral gas, and ν is the electron-neutral collision frequency. The last term represents the electron energy loss due to every inelastic collisional process i. ΔE_i is the threshold energy, and r_i is the rate of progress of the ith electron impact reaction.

These equations are discretized using the finite volume method in a segregated manner. First-order semi-implicit time-stepping is used along with the Scharfetter–Gummel (SG) scheme for the convection–diffusion flux. The SG scheme degenerates to a first order upwind scheme for the drift (convection) term in the limit of high Peclet numbers ($Pe = \mu_k |\vec{E}| dx/D_k$), i.e. when convection dominates over diffusion; and degenerates to a second-order central scheme for the diffusion term, in the opposite limit. The second-order central scheme is used for solving the Poisson equation for the electric potential ϕ. The linear solves are performed using an in-house GMRES (Generalized Minimum Residual Method) implementation, which uses the modified Gram–Schmidt algorithm for generating an orthonormal Krylov subspace basis. This

algorithm was also used in a 3D solver, described in Sitaraman and Grout [36]. The geometric multigrid method is used as the preconditioner for GMRES, and the Gauss-Seidel method is used as the smoother on successive multi-grid levels. This solver is named as Multi-grid Plasma Solver 1D (or 'mps1d' as is mentioned in this article)

2.2. Solver verification

Two popular cases in the literature, where both fluid and particle-in-cell (PIC) models have been employed and compared, are used as the verification targets for the mps1d code developed and used in this research. The first case is a capacitively coupled plasma with a radio frequency (RF) source in helium. And the second case is a negative (anode-directed) 1D streamer ionization front in nitrogen at atmospheric pressure. These cases are described in sections 2.2.1 and 2.2.2, respectively.

2.2.1. Capacitively coupled plasma discharge in helium. A capacitively coupled plasma discharge in Helium, driven by an RF source, has been simulated using mps1d. This case was presented as one of the four benchmark cases in Turner *et al* [37], where they performed detailed PIC simulations and compared the results using five independently developed PIC codes. An RF sinusoidal voltage with an amplitude of 120 V and a frequency of 13.56 MHz was used to generate a plasma in He at 1 Torr and 300 K. The inter-electrode gap was set to 6.7 cm, which was discretized using 513 uniformly spaced grid points with a fixed time step of 2.3×10^{-11} s. A uniform spatial plasma density of 3.8×10^{14} m^{-3} was used to initialize the ion and electron number densities. Maxwellian thermal flux boundary conditions were used for the electron density (8), neutral species density (9), and the mean electron energy density equations (10), whereas the drift-dominated flux boundary condition was used for the ion density equation (11). In equations (8)–(11), $\vec{\Gamma}_e$, $\vec{\Gamma}_n$, and $\vec{\Gamma}_i$ are the fluxes of electron number density, neutral species number density, and ion number density, respectively. Similarly, n_e, n_n, and n_i are the electron, neutral, and ion number densities, and m_e and m_n are the masses of the electron and the nth neutral species, respectively. Secondary electron emission at the boundaries due to the impacting ion flux is also accounted by specifying the secondary electron emission coefficient, γ. However, for this specific case, $\gamma = 0$. Also, the gas temperature (T_g) is held constant at 300 K in this verification case. Finally, the Dirichlet boundary conditions were used for the electric potential equation, as shown in equation (12), where the cathode potential (ϕ_c) was set to 0 and the anode potential (ϕ_a) was set to the applied RF voltage waveform

$$\vec{\Gamma}_e = \frac{1}{4} n_e \left(\frac{8k_B T_e}{\pi m_e} \right)^{1/2} - \gamma \vec{\Gamma}_i \tag{8}$$

$$\vec{\Gamma}_n = \frac{1}{4} n_n \left(\frac{8k_B T_g}{\pi m_n} \right)^{1/2} \tag{9}$$
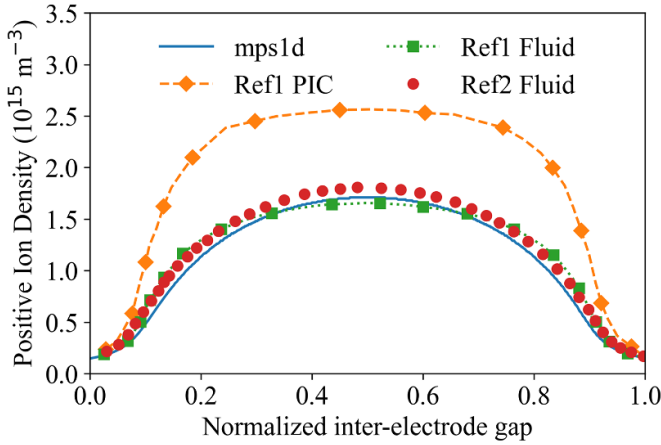
Figure 1. He$^+$ density comparison between mps1d and capacitive discharge benchmark results from Turner *et al* [37] (Ref1 PIC and Ref1 Fluid using PIC and fluid models) and with Verma and Venkattraman [38] (Ref2 Fluid).

$$\vec{\Gamma}_{E_e} = 2k_{\mathrm{B}}T_e\vec{\Gamma}_e \tag{10}$$

$$\vec{\Gamma}_i = \max\left(-\mu_i n_i \frac{\partial \phi}{\partial x}, 0\right) \tag{11}$$

$$\phi_a = \phi_0 \sin(2\pi f t), \phi_c = 0.0. \tag{12}$$

The chemical mechanism comprising of two electron impact excitation and ionization reactions of He was obtained from the cross section data provided by Turner *et al* [37] using an offline Boltzmann equation solver, BOLSIG+ [35]. The rate constants were obtained as functional fits of electron temperature. The ion mobility equation was obtained from Turner *et al* [37] while the electron mobility and diffusivity were also obtained as functions of the electron temperature from the aforementioned BOLSIG+ solver. These details have been provided in appendix A. These simulations were run for 0.1 ms, over which the difference in peak electron density between subsequent time-steps reduced by 5 orders of magnitude, indicating a steady state in plasma density. The average ion number density at steady state is shown in figure 1.

Reasonable agreement between the fluid model (mps1d) and moment results from Turner *et al* [37] was obtained. We also compared our solution with an OpenFOAM-based fluid model [38], which also indicates good agreement. The discrepancy between PIC and fluid solutions is a consequence of the formulation of electron impact rate and electron transport coefficients from the offline Boltzmann equation solver, and subsequent curve-fitting/tabulation to functions of reduced electric field (E/N) or mean electron energy. These differences are also attributed to the choice of ion, electron, and electron energy mobilities and diffusivities, and the boundary conditions. As is also mentioned in Turner *et al* [37], the transport coefficients and boundary conditions can play a major role in obtaining a desired level of accuracy using a fluid model

compared to the benchmark PIC simulation results for this low pressure capacitive discharge simulation.

2.2.2. Anode-directed streamer in nitrogen. Aligned with the motivation and conditions of this research, 1D streamer ionization front simulation results from mps1d have also been compared with published PIC and fluid model results for solver verification. Negative (anode-directed) streamers in nitrogen at 298 K and 1 atm were modeled and compared with the results from Markosyan *et al* [39]. This paper evaluates the accuracy of a higher order moment model, derived in Dujko *et al* [40], by comparing 1D streamer propagation results with PIC and a local field approximation (LFA) based drift-diffusion model. As is done in Markosyan *et al* [39], a 1.2 mm long 1D inter-electrode gap was chosen as the computation domain. 1025 uniformly spaced grid points were used to discretize this domain and a fixed time-step of 0.05 ps was used throughout the simulation. To maintain the same background reduced electric field of 590 Td, as is used in Markosyan *et al* [39], the anode potential was set to 17.3 kV and the cathode was grounded. Homogeneous Neumann boundary condition ($\partial_x n_e = 0$) at the anode ($x = 0$) and the Dirichlet boundary condition ($n_e = 0$) at the cathode ($n_e = 0$) for electron number density were used. However, these did not impact the results much, since the streamer front was fairly away from the boundaries for the duration of interest. A Gaussian seed of electrons and ions was used to initialize this simulation, as is given in equation (13), where $n_{e0/i0} = 2 \times 10^{18} \mathrm{m}^{-3}$, $\sigma = 0.029$ mm, and $x_0 = 0.8$ mm:

$$n_{e/i}(x)|_{t=0} = n_{e0/i0}\exp\left(\frac{-(x-x_0)^2}{\sigma^2}\right). \tag{13}$$

The local field approximation (LFA) was used, where the ionization rate coefficient, electron mobility, and diffusion coefficient were fit as functions of the local reduced electric field (E/N), based on the plots for all these quantities provided in Dujko *et al*'s paper [40]. The exact expressions used for these quantities have been provided in appendix A. The high background electric field (145 kV cm^{-1}) results in an electron-impact ionization that causes rapid growth in the electron and ion number density Gaussian seed. Subsequently, the electrons drift towards the anode, i.e. opposite to the direction of the applied field, whereas the heavier ions remain stationary within electron drift time-scales, thereby creating a space charge field. This starts to distort the constant electric field, as is seen in figure 2. Finally, the space charge created by the anode-directed drifting electrons and the cathode-directed 'very slow' positive ions screen the electric fields in the ionized region from the external field, which stops further ionization and begins the front propagation. The electric fields, electron and ion number densities at three time instances (0.07 ns, 0.35 ns, and 0.7 ns) are compared with the PIC (Ref PIC) and the drift-diffusion (Ref DD) model results from Markosyan *et al* [39] in figures 2–4, respectively.
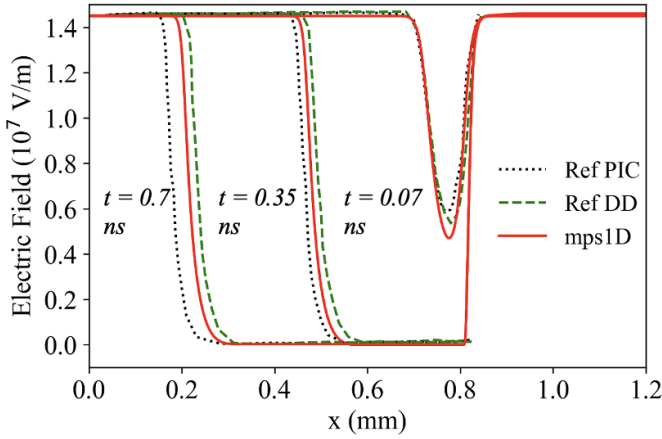
Figure 2. Electric Field Comparison between mps1d, drift-diffusion model (Ref DD) results and PIC results (Ref PIC) from Markosyan *et al* [39]. Anode—electrode at $x = 0$ mm.
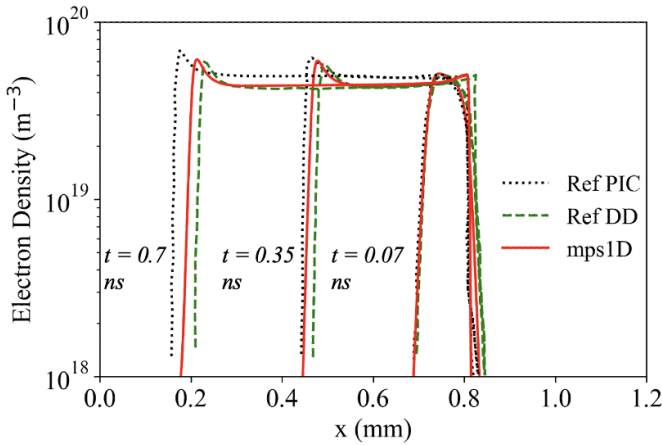
Figure 3. Electron Number Density Comparison between mps1d, drift-diffusion model (Ref DD) results and PIC results (Ref PIC) from Markosyan *et al* [39]. Anode—electrode at $x = 0$ mm.
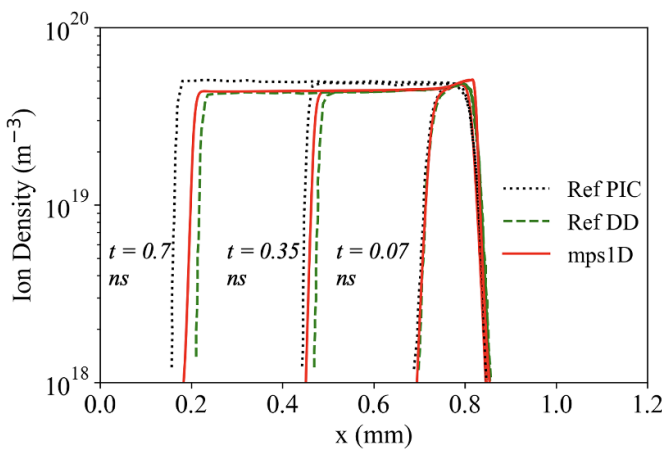
Figure 4. Ion Number Density Comparison between mps1d, drift-diffusion model (Ref DD) results and PIC results (Ref PIC) from Markosyan *et al* [39]. Anode—electrode at x = 0 mm.

Results from mps1d agree quite well with the drift-diffusion model results. However, there are some variations when compared to the PIC simulation results as time progresses, which are primarily due to the assumption that the mean electron energy relaxation is instantaneous (LFA), based on the local electric field in the drift-diffusion models with LFA. However, the high cost associated with using detailed plasma mechanisms, as is used in this research (section 3) with higher order models and particle models, especially in higher dimensions, make the drift-diffusion model a viable choice for streamer simulations.

3. Results and analysis

This section presents 1D avalanche to streamer transition and streamer propagation simulations in atmospheric-pressure ammonia-oxygen-nitrogen-water ($NH_3/O_2/N_2/H_2O$) mixtures using nanosecond non-equilibrium plasma. The applicability of the Meek's criterion [29, 30] for streamer inception is first evaluated. Emphasis has also been laid on the electron energy budgets to understand the pathways for the production of important radicals for combustion during the streamer propagation phase.

3.1. Applicability of meek's criterion for streamer inception

All streamer simulations presented in this section were initialized with a very low uniform density of electrons and ions (100 electrons or ions cm^{-3}). Thus, the avalanche phase, where the electrons drift from the cathode to the anode due to the applied electric field which causes successive ionization and production of more free electrons, has also been modeled. In order to prevent the electrons from diffusing out of the domain from the cathode, due to the Maxwellian thermal flux boundary condition, secondary electron emission has been accounted for in the boundary condition for electron density evolution. These secondary electrons not only create an extra source of electrons at the boundary to sustain the avalanche, but also help in faster streamer propagation by increasing the number of ionization events downstream of the ionization wave. The flux of the secondary electrons is calculated by incorporating the flux ($\gamma \vec{\Gamma}_i$) as is done in equation (8). The secondary electron emission coefficient was chosen as 0.01 assuming the target electrode material as copper and the gas as air (This value is an upper limit for Cu and N_2 combination at atmospheric pressure as per [41]). Similarly, boundary condition for the electron energy flux accounts for the energy of the ejected secondary electrons based on the ion impact energy (evaluated as $\Sigma_i 0.5 m_i v_{d,i}^2 - W_c$, where m_i is the mass and $v_{d,i}$ is the drift velocity of the incident i^{th} ion, and W_c is the work function of the assumed copper electrode $\sim$4.65 eV).

The avalanche transitions to a streamer only if the electrons have a sufficiently high mean energy to cause sustained ionization, which can eventually result in a space charge field that is greater than the breakdown field of a gas. The location of streamer inception can be obtained from the Meek's criterion

J. Phys. D: Appl. Phys. **58** (2025) 015204

T S Taneja *et al*

[29, 30], which is given by:

$$\int_0^{z_0} \bar{\alpha}\left(z, E_0\right) \mathrm{d}z = K. \tag{14}$$

Here, $\bar{\alpha}$ is the effective ionization coefficient: i.e. $\bar{\alpha} = \alpha - \eta$, with α being the ionization coefficient and η being the attachment coefficient. z_0 is the location of streamer inception relative to the cathode, E_0 is the applied background electric field, z represents the distance along the avalanche path relative to the cathode, and K is a constant which is typically between 18 and 20 [41]. Specifically, the streamer inception location (z_0) is defined as the location where the first local maximum in $log(n_e(x))$ is observed post its departure from a straight line, which represents exponential avalanche. Value of K has been observed to be around 20 for pure air at atmospheric pressure in experiments [41]. Equation (14) can be simplified to $\bar{\alpha}z_0 = K$, if $\bar{\alpha}$ is assumed to be independent of the background electric field and the location.

1D simulation with a constant background field applied to a stoichiometric mixture of NH_3 / O_2 / N_2, at a constant pressure of 1 atm and a constant gas temperature of 300 K was first conducted to check the validity of Meek's criterion for streamer inception. 2049 grid points have been used to divide the domain with a uniform cell size of 1.95 μm. A constant time-step size of 0.05 ps was used for all the simulations. The plasma kinetic mechanism used in these simulations has been derived from an experimentally validated ammonia oxidation mechanism by Zhong *et al* [6]. This mechanism has 27 species, comprising of background species (i.e. NH_3, N_2, O_2, and H_2O), ions, electronically excited states, and radicals produced, due to 81 total reactions spanning electron impact electronic excitation, ionization, attachment, dissociation, charge exchange, recombination, and quenching. The ZDPlasKin-version input file of the kinetic mechanism and the cross sections (obtained from LxCAT and derived from Zhong *et al* [6]) has been provided in the supplementary materials. All heavy species are assumed to remain stationary, whereas electron density and mean electron energy are assumed to follow the drift-diffusion approximation. Appropriate source terms listed in section 2.1 have also been accounted for obtaining the solutions.

The anode ($x = 0$) was held at a constant potential of 11.5 kV whereas the cathode ($x = 4$ mm) was grounded. The interelectrode gap was 4 mm. This resulted in a background field of 28.75 kV cm^{-1}, which is close to the breakdown field of pure air (ranging between 26–31 kV cm^{-1} at STP [41]). This corresponds to a background reduced electric field (E/N) of ~118 Td. The mole fractions at stoichiometric conditions are $NH_3 : O_2 : N_2 = 0.2188 : 0.1641 : 0.6171$. At these conditions, the effective ionization coefficient $\bar{\alpha}$ obtained from BOLSIG+ is ~5980 m^{-1}: i.e. 5.98 mm^{-1}.

Figures 5 and 6 show the evolution of the electron number density in space at different time instances. The applied nanosecond pulse is turned off after the streamer connects the electrodes, as the aim is to model avalanche to streamer transition and propagation phases only. figure 5 shows the first phase of the evolution: i.e. the avalanche phase where the electrons
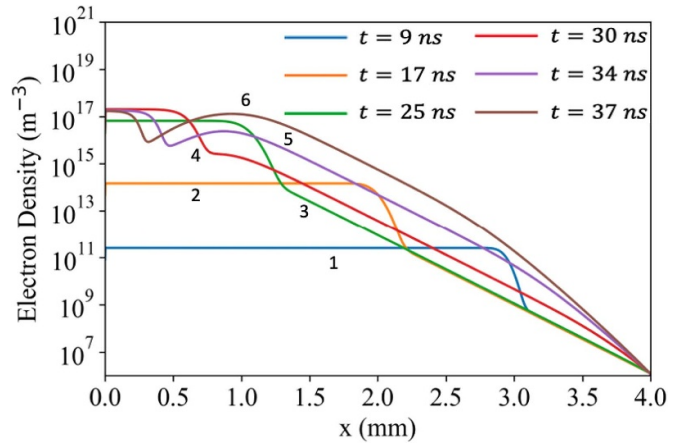
Figure 5. Avalanche Phase—Electron number density evolution. Integer numbers marked in the plots aid in showing the temporal sequence of the evolution..
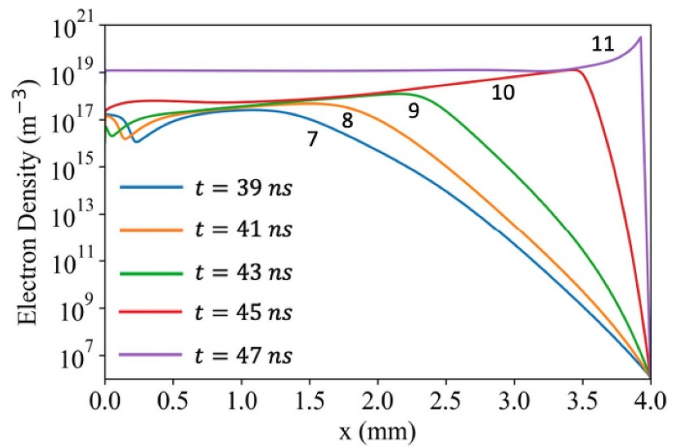
Figure 6. Streamer Propagation Phase—Electron number density evolution. Integer numbers marked in the plots aid in showing the temporal sequence of the evolution..

drift towards the anode and multiply, starting from a low initial electron number density of 10^8 m^{-3}. The integer numbers marked in this figure aid in tracking the temporal evolution, which can also be seen from the legend of the plot.

The natural logarithm of the electron density is plotted in figure 7. The profiles at the initial time instances (9 ns, 17 ns, 25 ns) fall on a straight line in this plot, which confirms the exponential increase in electron density as per Townsend's theory of electron avalanche. Since the background field is slightly higher than the breakdown field, bulk ionization is also observed in addition to electron drift and subsequent multiplication. The abscissae and ordinates marked in figure 7 help in determining the slope of these lines, graphically. As can be easily deduced, the slope is ~6.38 mm^{-1}. As per equation (15), this slope is equal to the Townsend's effective ionization coefficient $\bar{\alpha}$.

$$n_e = n_{e0}\exp\left(\bar{\alpha}d\right),$$
$$\log_e n_e = \log_e n_{e0} + \bar{\alpha}d. \tag{15}$$
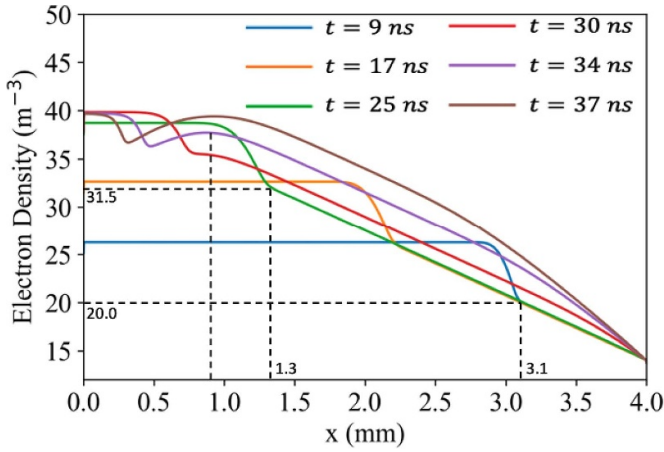
Figure 7. Logarithm of electron number density. Abscissae and ordinates marked near respective dashed lines.

Thus, there is only a 6.6% difference in the values of $\bar{\alpha}$ obtained from BOLSIG+, and graphically, from the simulations performed using mps1d. Furthermore, using the value obtained from the plots, i.e. $\bar{\alpha} = 6.38$, the Meek's criterion suggests that the distance of streamer inception should be given by, $\bar{\alpha}d = K(K = 18 - 20)$: i.e. $d = 2.82 - 3.13$ mm from the cathode. As can be seen from figure 7, the streamer head, indicated by a deviation from the linear trend, first forms at 34 ns and a distance of 0.9 mm from the anode (i.e. 3.1 mm from the cathode), which is within the range predicted by the Meek's criterion. Figure 6 shows the streamer propagation phase where the cathode directed streamer propagates under the influence of the space charge field and the background electric field. The streamer head is defined by the location of the maximum gradient in electron number density. Instantaneous streamer head velocities at a given head location, x_i are evaluated as $dx/dt|_{x_i}$ and have been listed in table 1. As can be seen, the streamer velocities rise by more than an order of magnitude since inception till they bridge the inter-electrode gap, which is a consequence of the increasing resultant reduced electric field at the streamer head. This increases the electron impact ionization rates, which is the primary mechanism for streamer propagation in positive streamers. The pulse was turned off at 47 ns in this case, when the streamer head reached the cathode. Figure 8 shows the evolution of the reduced electric field in the 1D domain. It remained constant at 118 Td (corresponding to an electric field of 28.75 kV cm^{-1}) until the space charge field started to distort the external applied field, at 34 ns, resulting in reduction of the electric field behind the streamer head, due to the opposing combination of the space charge field (directed right to left, behind the streamer head) and the background field (directed left to right). The same reason led to the increase of the electric field at and ahead of the streamer head, since the positively charged streamer head is at a higher potential than the cathode potential, resulting in a field that points in the same direction as the background field. Unlike most 2D and 3D fluid plasma simulations, field enhancement at the streamer head due to its

Table 1. Instantaneous streamer head velocities tabulated with time and the instantaneous streamer head location.

| Time (ns)	Head location (mm)	Head velocity (m/s)
34	0.90	7.73×10^4
41	1.75	2.38×10^5
44	3.00	4.21×10^5
45	3.50	4.86×10^5
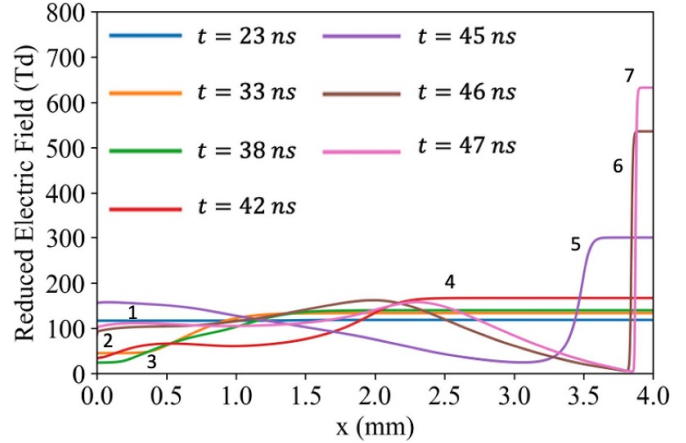
Figure 8. Streamer Formation and Propagation—Reduced Electric field evolution in the mixture of reactants at 300 K. Integer numbers marked in the plots aid in showing the temporal sequence of the evolution.

curvature, can not be captured in a 1D simulation. Thus, the field ahead of the streamer head remains constant till the cathode (which can be seen clearly at $t = 38$ ns to $t = 47$ ns in figure 8).

3.2. Streamers at Ammonia-Air Flame Conditions: Effect of the Thermochemical State

Our verified plasma fluid model was further used to simulate 1D streamers at ammonia-air flame conditions. Every subsequent plasma pulse in a series of high-frequency repetitively pulsed discharges in combustible mixtures used for igniting and stabilizing flames are deposited in an evolving background temperature and composition. The effect of the thermochemical state on the plasma streamer kinetics and dynamics has been modeled by assuming that states along a 1D laminar premixed flame are representative of such evolving environments. Particularly, the avalanche to streamer transition, streamer propagation, and the production of important radicals have been investigated. Four different states along the solution of a one-dimensional, freely propagating, laminar, premixed ammonia-air flame, modeled using Cantera [42], are chosen as the initial conditions for streamer simulations. These are marked by stars in figure 9, which show the temperature, and mole fractions of four major species, NH_3, O_2, N_2, and H_2O along the flame. These have also been tabulated in table 2.

These thermochemical states are points in the unburnt reactants, the pre-heat zone, the the reaction zone, and the
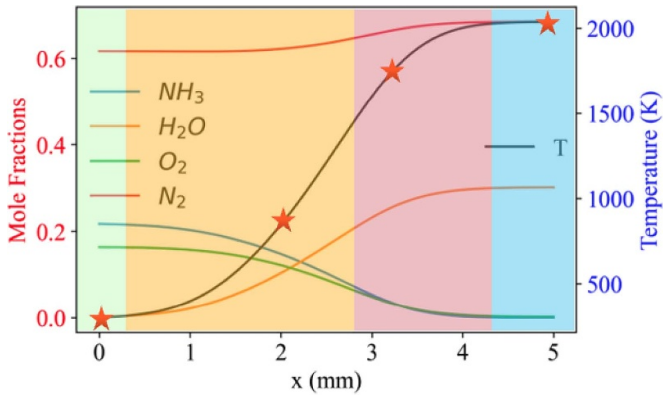
Figure 9. 1D laminar, freely propagating, premixed NH_3-air flame structure (major species mole fractions and temperature). Red stars represent 4 thermochemical states used for streamer simulations.

Table 2. Temperature and mole fractions of the four thermochemical states marked in figure 9.

| No.	Temp(K)	X_{NH_3}	X_{O_2}	X_{N_2}	X_{H_2O}
1	300	0.2188	0.1641	0.6171	0.0
2	900	0.1411	0.1170	0.6290	0.1129
3	1600	0.0530	0.0479	0.6674	0.2317
4	2037	0.0	0.0	0.6988	0.3012

burnt products, as is marked in figure 9 using different background colors (green, yellow, red, and blue, respectively). The reactants are heated in the pre-heat zone due to diffusion of heat from the reaction zone, whereas the chemical heat release happens in the reaction zone. This flame is at a stoichiometric equivalence ratio, where complete combustion of ammonia in air is governed by $NH_3 + 0.75(O_2 + 3.76N_2) \longrightarrow 3.32N_2 + 1.5H_2O$. While there are intermediate reaction steps which involve the production and consumption of other minor species, their mole fractions are typically small, and thus, any electron-impact reactions due to the presence of minor species has been neglected.

Streamer simulations with the premixed reactants have been shown in the previous sub-section. The avalanche to streamer inception time was 34 ns, whereas the streamer propagation and connection time was 13 ns (with respect to the streamer inception instant) in the mixture of reactants at 300 K, with an applied voltage of 11.5 kV. Streamer inception instant is defined as the instant when a local maximum is first observed in the electron number density post its departure from a straight line. The connection instant is denoted when the streamer head first reaches near the cathode.

Figures 10–12 show the evolution of the electron number density for the three other thermochemical states at temperatures of 900 K, 1600 K, and 2037 K, respectively, all at a constant pressure of 1 atm. A drastic reduction in both the avalanche to streamer transition time and the streamer propagation & connection time can be seen. Streamer inception happens at 16 ns (900 K, pre-heat zone), at 6.5 ns (1600 K, reaction zone) and at 4.6 ns (2037 K, burnt products); whereas the streamers connect the two electrodes after an additional 3
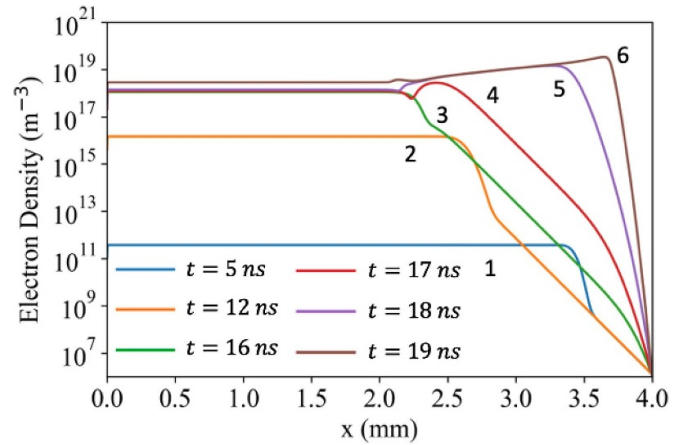
Figure 10. Streamer Inception and Propagation at 900 K (pre-heat zone) - Electron Number Density.
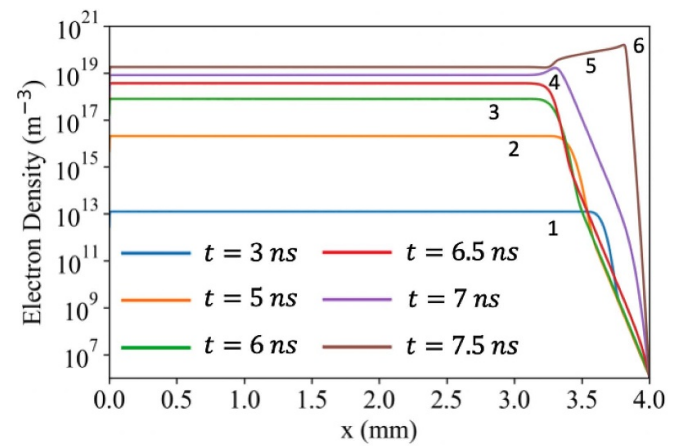
Figure 11. Streamer Inception and Propagation at 1600 K (reaction zone) - Electron Number Density.
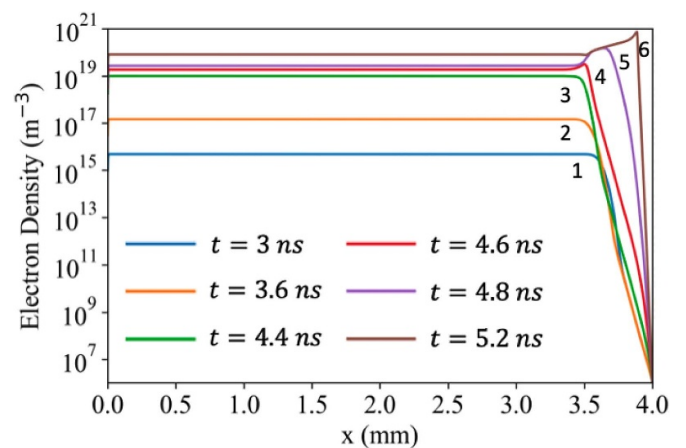
Figure 12. Streamer Inception and Propagation at 2037 K (burnt products) - Electron Number Density.

ns (900 K, pre-heat zone), 1 ns (1600 K, reaction zone) and 0.6 ns (2037 K, burnt products). The streamer inception location at these three other thermochemical states can also be deduced
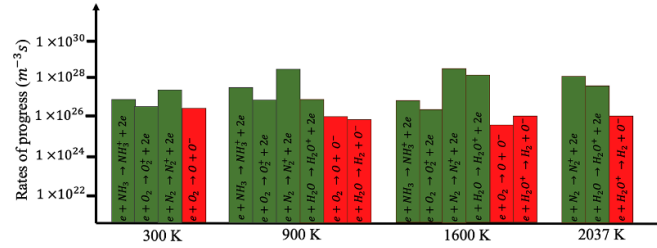
Figure 13. Averaged rates of ionization (green bars) and attachment (red bars) reactions at the streamer head.
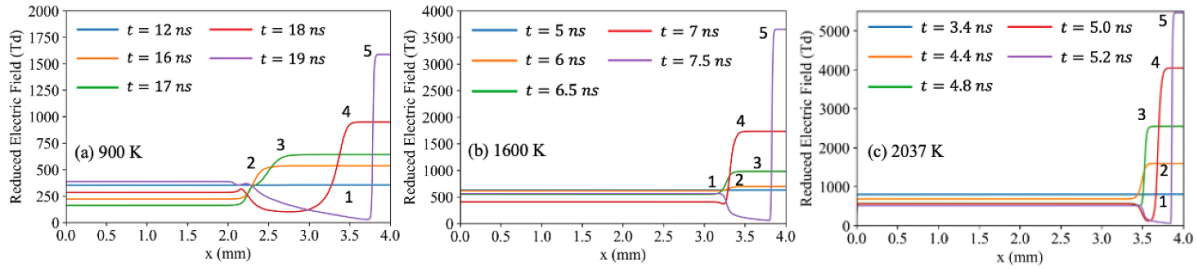

Figure 14. Evolution of the reduced electric field in the (a) pre-heat zone, (b) reaction zone and (c) burnt product zone mixtures.

from the Meek's criterion, as is done in the previous subsection. The velocity of a positive streamer simply depends on the net ionization rate, which keeps driving the front toward the cathode. The ionization rate is a non-linear function of the reduced electric field (E/N).

Figure 13 shows the rates of progress of the different ionization and attachment reactions that directly contribute to the production or consumption of electrons. These rates are temporal averages of the rates at the streamer head, between instances of streamer inception and streamer connection. Since the voltage is held constant at 11.5 kV for all the cases, the background E/N varies inversely with the background gas number density. The evolution of the E/N in the reactant mixture was shown in figure 8. The evolution of E/N at the three other thermochemical states is shown in figure 14. As is seen from this figure and figure 8, the reduced electric field at the streamer head increases by more than an order of magnitude as the thermochemical state changes from the reactant mixture at 300 K to the burnt product mixture at 2037 K. As can also be seen from these plots, the reduced electric field before the breakdown simply scales with the inverse ratio of temperatures from one state to another, with values of 354 Td, 630 Td and 800 Td, respectively. Local minima in the reduced electric field in the streamer tail is also captured in figure 8, which are caused by the redistribution of charged species (both ions and electrons) in a way that opposes the external electric field, effectively screening it within the streamer tail. Given the non-linear dependence of the reaction rate coefficients on the E/N, the rates of ionization of N_2 increase by more than 5X as the thermochemical states are varied from the reactants at 300 K to the burnt products at 2037 K. A similar rise in the ionization rates of H_2O can also be seen from the rate in the pre-heat zone to the rate in the burnt products. Despite the reduction in the overall densities of N_2 and H_2O with increasing temperature, the ionization rates were found to be highest in the

burnt products, due to higher ionization rate coefficients which increase non-linearly with the reduced electric field. The rates of ionization of O_2 and NH_3 increase by a factor of ~ 2 from the thermochemical states in the reactants to those in the preheat zone, but dwindle in the reaction zone due to the lower mole fractions and number densities of NH_3 and O_2 at this state. Furthermore, the dissociative attachment reactions of O_2 ($e + O_2 \longrightarrow O + O^-$) and $H_2O(e + H_2O \longrightarrow H2 + O^-$) were also found to consume electrons at the streamer head, but the rates of ionization are almost 1–2 orders of magnitude higher, which results in net ionization wave propagation towards the cathode. This shows that ideally, the applied voltage and/or the pulse duration should be adaptive in a practical combustor using nanosecond pulsed plasma for ignition or flame stabilization, based on the expected local thermochemical state in the volume of the discharge. This will not only result in ignition energy savings, but will also prevent undesirable arcing which can release excessive heat and damage the electrodes.

Next, the background E/N was made equal for all the cases by reducing the applied voltage at the anode by scaling it inversely with the total number density. This was done to see the effect of the gas composition alone, without affecting the rates by the reduced electric field (E/N). Figure 15 shows that only the discharge in the reactants led to the formation of a streamer at 34 ns. Failure of breakdown was observed in all the three other thermochemical states. Few electrons are lost at the cathode due to the Maxwellian thermal flux boundary condition despite secondary emission, while the other electrons keep drifting towards the anode, without any multiplication, and are eventually lost at the anode. This shows that the gas composition alters the effective ionization coefficient $\bar{\alpha}$, which governs the critical breakdown field. For instance, the effective ionization coefficient was found to be negative at the three other thermochemical conditions of the pre-heat (900 K), reaction (1600 K) and burnt products (2037 K) zones at a reduced
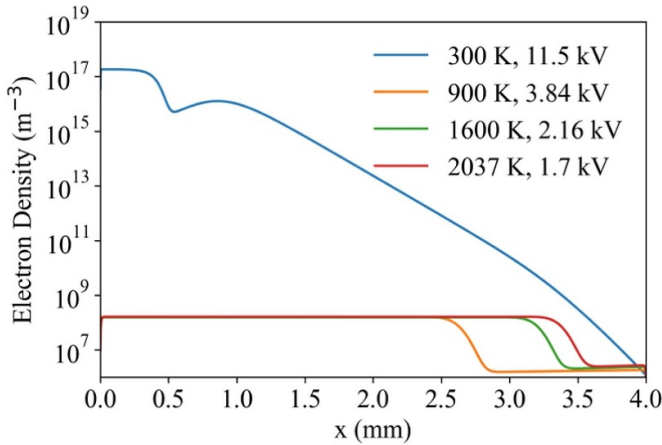
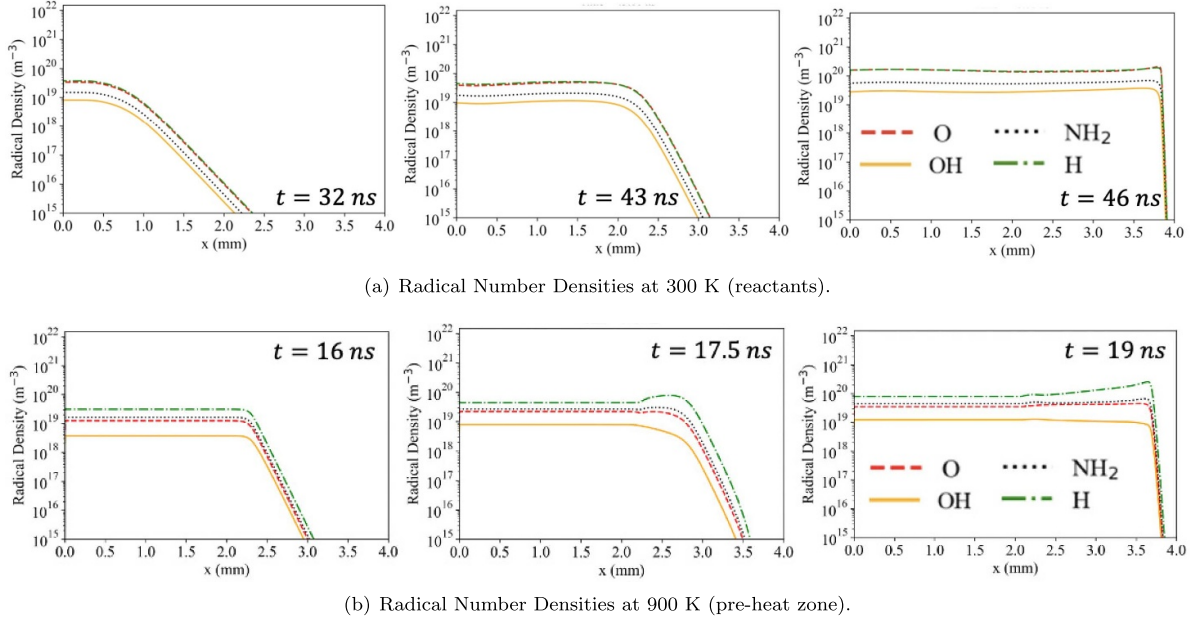**Figure 15.** Comparison of electron number density evolution for the four thermochemical states at 34 ns.

electric field of 118 Td. Values of $\bar{\alpha}$ at the three states are -184 m^{-1}, -642 m^{-1} and -1093 m^{-1}, respectively. As a result, breakdown at these conditions was not observed. This is a consequence of the difference in the way electron energy is distributed in different gas mixtures through excitation, dissociation, attachment and ionization pathways at a given external reduced electric field.

Next, we probe into the production of radicals such as O, H, and OH, which trigger the chain initiation and branching reactions of combustion, for ignition and flame stabilization objectives. We also look at NH$_2$, which is an important radical that can either contribute to the production of NO via NH$_2 \longrightarrow$ H2NO $\longrightarrow$ HNO $\longrightarrow$ NO at the instance of ignition, or assist in reducing NO by NH$_2$ + NO $\longrightarrow$ NNH + OH and NH$_2$ + NO $\longrightarrow$ N$_2$ + H$_2$O post-ignition. The chemical kinetics governing these phenomena were uncovered in our article on plasma assisted combustion of ammonia-air mixtures [8]. Since these radicals are mainly of interest to lower the activation energy for the reactions in the pre-heat zone of the flame, we only perform this analysis at two states that precede the conditions of the reaction zone: the reactants at 300 K and the mixture in the pre-heat zone at 900 K. Figures 16 (a) and (b) show the densities of these radicals at the two states, at three time instances: at the instance of streamer formation, during streamer propagation, and immediately before streamer connection (immediately after the supply voltage is turned off). The following analysis is based on the net production rate data at three spatial locations along the streamer path. The O radicals are predominantly produced by the electron impact dissociation reaction of e + O$_2 \longrightarrow$ e + 2O and the dissociative electronic excitation reaction of e + O$_2 \longrightarrow$ e + O + O(^{1}D) during the avalanche and the streamer propagation phases. An order of magnitude rise in the O number density is also seen immediately after the pulse is turned off which is due to the quenching of the electronic excited states of N$_2$, mainly via N$_2$(B3) + O$_2 \longrightarrow$ N$_2$ + 2O. This reaction also results in fast gas heating, which has not been modeled currently. At 900 K

(pre-heat zone), the lower mole fraction and overall number density of O$_2$ suppresses the rates of these reactions, which results in a final O radical number density of $\sim 4 \times 10^{19}$ m^{-3} as compared to $\sim 2 \times 10^{20}$ m^{-3} produced in the reactant mixture at 300 K. A recent paper by Sun *et al* [43] performed LIF measurements of O and OH in NH$_3$-air flames. Based on their measurements, they proposed the same dominant pathways for O radical production as described here.

OH production in the reactant mixture at 300 K happens solely due to the dissociative quenching of O(^{1}D) with NH$_3$: i.e. O(^{1}D) + NH$_3 \longrightarrow$ OH + NH$_2$. Whereas in the pre-heat zone mixture at 900 K, two additional pathways also contribute to OH production. The first being the electron impact dissociation of H$_2$O, e + H$_2$O $\longrightarrow$ e + H + OH, and the second being the dissociative quenching of O(^{1}D) with H$_2$O, O(^{1}D) + H$_2$O $\longrightarrow$ 2OH. However, these two reactions together contribute only about 20% to the total production of OH at 900 K, and only during the streamer inception and propagation phases: i.e. data obtained at $t = 16$ ns and 17.5 ns. The rest is produced due to O(^{1}D) + NH$_3 \longrightarrow$ OH + NH$_2$. The lower mole fraction and density of O$_2$ and NH$_3$ at 900 K, affect the production of OH, resulting in a 2.5X decrease in total OH yield after the streamer reaches the cathode ($\sim 1 \times 10^{19}$ m^{-3}) as compared to the case at 300 K ($\sim 2.5 \times 10^{19}$ m^{-3}). Experiments and analysis in Sun *et al* [43] suggested O + NH$_3 \longrightarrow$ OH + NH$_2$ as the dominant pathway for OH production in the unburnt state and O + H$_2$O $\longrightarrow$ 2OH in the burnt state. It should be noted that O here refers to both the ground state O(^{3}P) and the excited state O(^{1}D). However, since their analysis was conducted after 400 ns, i.e. in the nanosecond spark phase only, which happens much longer after the pulse was turned off, the direct electron impact ionization pathway of e + H$_2$O $\longrightarrow$ e + H + OH was not found to be a major pathway to produce OH radicals. However, during the streamer formation and propagation phases, this pathway contributes around 10% to the total OH production. Finally, given the much lower rate constant of N$_2$(A) + H$_2$O $\longrightarrow$ N$_2$ + H + OH [44, 45] compared to all other OH production pathways, this reaction was not found to be an important pathway for OH or H production in the pre-heat, reaction or the burnt products zones. This fact was also emphasized in [43].

H radicals are almost completely produced due to electron impact electronic excitation of NH$_3$ and its subsequent dissociative quenching at 300 K in the reactant mixture. The two electronic excitation processes are e + NH$_3 \longrightarrow$ e + NH$_3$(e1) and e + NH$_3 \longrightarrow$ e + NH$_3$(e2). NH$_3$(e1) and NH$_3$(e2) instantaneously quench to form NH$_2$, H, and NH. Since quenching is considered to be instantaneous, these two-step processes are clubbed into e + NH$_3 \longrightarrow$ e + NH$_2$ + H and e + NH$_3 \longrightarrow$ e + NH + 2H, where the excitation rate coefficients for the production of NH$_3$(e1) and NH$_3$(e2) have been used, respectively. In addition to this pathway, at 900 K (pre-heat zone), about 10% of the H radicals are also produced by the direct electron impact dissociation reactions of e + H$_2$O $\longrightarrow$ e + H + OH. Overall, the H radical densities

(a) Radical Number Densities at 300 K (reactants).

(b) Radical Number Densities at 900 K (pre-heat zone).

Figure 16. Number densities of O, OH, H, and NH$_2$ radicals during the avalanche, streamer formation, and propagation phases.

remained fairly identical in the unburnt reactant and pre-heat zone mixtures.

NH$_2$ radicals are also produced predominantly by the same reaction, $\mathrm{e + NH_3 \longrightarrow e + NH_2 + H}$ at both the thermochemical states during the streamer formation and propagation phases. However, due to the higher densities of $\mathrm{O(^1D)}$ towards the end of streamer propagation, especially in the reactant mixture at 300 K, $\mathrm{O(^1D) + NH_3 \longrightarrow OH + NH_2}$ contributed almost 30% of the total production of NH$_2$.

Given the crucial role of the electron impact reactions and the subsequent relaxation reactions in producing these radicals, the fractions of the total input energy used to facilitate these collisions were evaluated. Owing to the short mean free paths for heavy species at 1 atm, ion Joule heating was negligible (less than 0.5% of the electron Joule heating). Thus, the input energy is represented in the form of electron Joule heating. Fractions of this energy used in elastic and inelastic collisions were calculated to understand how the thermochemical state affects these distributions and how these fractions evolve over time and space in cathode-directed streamers. Equations (16) and (17) provide the definition of the elastic and inelastic loss fractions.
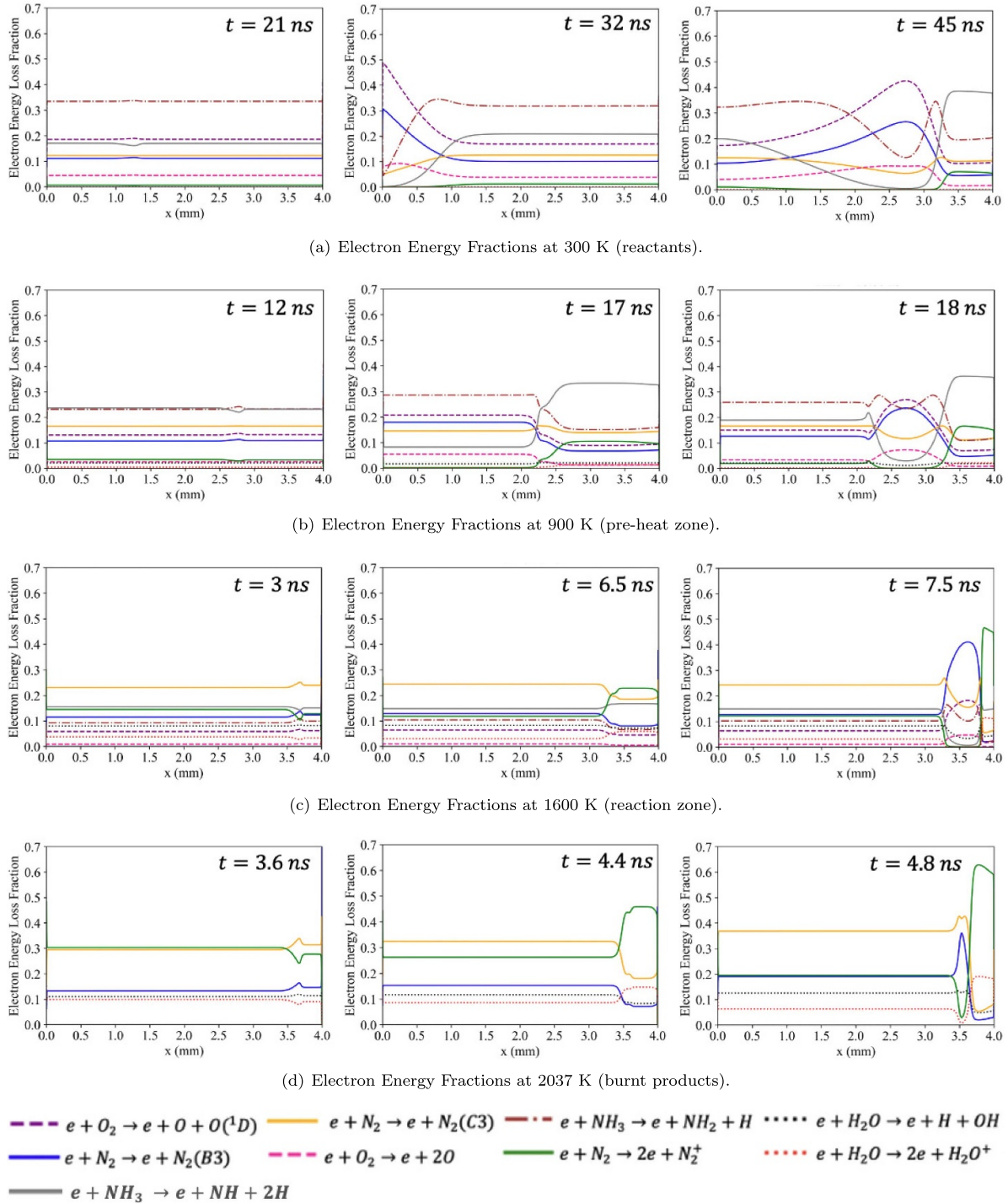
$$f_e = \frac{3}{2} n_e k_{\mathrm{B}} \left(T_e - T_g \right) \frac{2m_e}{m_b} \nu \frac{1}{e \vec{\Gamma}_e \cdot \vec{E}} \quad (16)$$

$$f_i = \frac{\Delta E_i r_i}{e \vec{\Gamma}_e \cdot \vec{E}}. \quad (17)$$

Less than 1% of the total electron Joule heating was spent in elastic collisions with the heavy species, given that the background reduced electric field (E/N) ranged between 118 Td to 800 Td. Hence, these fractions have not been shown in figure 17. The nine highest inelastic collision loss fractions have been plotted in the 1D space at three instances: during the avalanche, during streamer formation, and when the streamer

almost reaches the cathode. Figures 17(a)–(d) show these fractions at all the four thermochemical states of the 1D premixed ammonia-air flame. The legend has been provided at the bottom of this figure. Followings are the most important conclusions from these plots:

- The production of $\mathrm{O(^1D)}$ through $\mathrm{e + O_2 \longrightarrow e + O + O(^1D)}$ requires 18% energy during the avalanche phase, which increases to beyond 45% at the propagating streamer head in the reactant mixture at 300 K. This value reduces to almost 12% during avalanche and ranges between 20%–30% during the streamer propagation phases in the pre-heat zone mixture at 900 K. It further reduces to almost 5% during avalanche and ranges between 10%–20% during streamer propagation in the reaction zone mixture at 1600 K. This reaction is missing in the burnt products as there is no oxygen left after combustion. Moreover, this reaction takes precedence over another electron impact dissociation reaction, $\mathrm{e + O_2 \longrightarrow e + 2O}$, both of which produce O radicals, although with different threshold energies of 5.6 eV and 8.4 eV, respectively. Hence, given the importance of $\mathrm{O(^1D)}$ in the production of key radicals such as O, OH, and NH$_2$, it is worth noting that its spatio-temporal energy loss fraction evolves with the mixture conditions.

- The sum of the energy loss fractions of electronic excitation of N$_2$, to produce the two most dominant states, N$_2$(B3) and N$_2$(C3), remains between 20%–50% throughout the streamer evolution, at all the four thermochemical states. As is expected of a positive streamer, ionization of N$_2$ amplifies at its head, resulting in consuming almost 65% of the total input electron energy when the streamer reaches the cathode at the 2037 K case, which has the highest background reduced electric field. The increase in the ionization loss fraction of N$_2$ at the streamer head from the reactants to the

(a) Electron Energy Fractions at 300 K (reactants).

(b) Electron Energy Fractions at 900 K (pre-heat zone).

(c) Electron Energy Fractions at 1600 K (reaction zone).

(d) Electron Energy Fractions at 2037 K (burnt products).

Figure 17. Electron energy loss fractions during the avalanche phase (left), avalanche to streamer transition (middle), and when the streamer propagates and reaches the cathode (right), for all the four thermochemical states.

burnt products scales mainly with the higher electron temperature which in turn varies proportionally with the reduced electric field.

- Unlike what is often done in the development of phenomenological models [46–48] for plasma assisted combustion, the energy loss fraction for the fuel species in this case cannot be ignored. This is evident from the energy loss fraction of the electron impact excitation and

dissociation of NH_3 via $e + NH_3 \longrightarrow e + NH_2 + H$ and $e + NH_3 \longrightarrow e + NH + 2H$, which consumes ~50% of the total input electron energy during the avalanche phase for the streamers and can account for up to 25% of the total input energy in the propagating streamer head, in the reactant mixture. It is particularly important to account for these two processes, as they are primary steps for the production of H and NH_2 radicals.

- Similarly, it is important to consider the electron energy being spent on dissociating and ionizing H_2O, which is a product of ammonia combustion. Almost 5%–7% of the energy in the pre-heat zone mixture (figure 17(b)) and 10%–15% in the reaction zone mixture (figure 17(c)) was spent on these processes.

4. Conclusion

A 1D plasma fluid model has been developed and verified in this work, and is further used to simulate avalanche to streamer transition and streamer propagation in various background gas temperature and compositions at atmospheric pressure. The applicability of the Meek's criterion in determining the streamer inception location has been successfully confirmed for a premixed stoichiometric NH_3/air mixture. The streamer inception location was also observed to fall in the range predicted by the Meek's criterion. Next, a premixed ammonia-air freely propagating flame solution was used to represent the continuously evolving thermochemistry in a combustor, where non-equilibrium plasma is used for ignition and flame stabilization purposes. Streamer formation and evolution at four different conditions along the flame solution–(i) 300 K, reactants, (ii) 900 K, pre-heat zone, (iii) 1600 K, reaction zone, and (iv) 2037 K, burnt products. The avalanche to streamer transition time and the time taken by the streamer to propagate from the location of its inception to the cathode varied significantly from the 300 K reactant state to the 900 K pre-heat zone state. These durations further reduce at the 1600 K and the 2037 K states. This was attributed to the reduction of the total gas number density along the flame solution, which resulted in enhanced reduced electric field (E/N), causing faster ionization of NH_3, O_2, N_2, and H_2O. This observation motivated the use of adaptive voltage and pulse duration for practical combustors using multiple nanosecond pulsed plasma for ignition and flame stabilization, depending on the local thermochemical state. This information can also help in deciding the pulse interval to prevent excessive current supply which can damage the electrode surfaces. Moreover, using a 1D model also serves as a quick option to gain insight, which can guide detailed 2D axisymmetric or 3D streamer simulations in actual combustor configurations, and reduce the time spent in navigating through the entire set of design of experiments. The evolution of important radicals, such as O, OH, H, and NH_2 was investigated in the reactant and pre-heat zone mixtures. It was found that the dissociative electronic excitation of O_2 to form $O(^1D)$, contributed either directly or indirectly towards the production of O, OH, and NH_2 radicals. The role of the electronic excitation and subsequent dissociation of NH_3 to form NH_2 and H radicals was also found to be a dominant pathway, especially during the streamer formation and propagation phases. Finally, fractions of the electron Joule heating directed towards inelastic collisions were plotted during the avalanche, streamer propagation, and connection phases. Notable differences in the fractions for the production of $O(^1D)$ via electron impact on O_2 were observed spatio-temporally, as well as across different thermochemical states. Moreover, the

significance of accounting for the dissociation of the fuel species (NH_3) as well as combustion products (H_2O) has been emphasized. Future research will focus on modeling the combustion phase along with the plasma dynamics, where gas heating due to quenching of excited states of the background gases, coupled with radical generation from the plasma will be modeled. Time scales associated with these processes at different thermochemical states will also be uncovered in our future work.

Data availability statement

Acknowledgments

Author contributions

TST—Conceptualization, Data Curation, Formal Analysis, Investigation, Methodology, Software, Validation, Visualization, Writing—original draft. **HS**—Conceptualization, Investigation, Methodology, Software, Supervision, Validation, Writing—review and editing. **SY**—Conceptualization, Investigation, Methodology, Funding Acquisition, Project administration, Resources, Supervision, Writing—review and editing

Appendix. Reaction rate coefficients and transport coefficients used in the verification cases for mps1d

The list of reactions and their rate coefficients used in the He capacitive discharge verification case have been listed in table A1.

Table A1. Reactions, rate coefficients and electron energy exchange for the He CCP discharge case [37].

No.	Reaction	Rate coefficient (K, m, molecules)	Energy (eV)
R1	$e + He \longrightarrow He^* + e$	$(1.0 \times 10^{-14})\exp(-3.71344 \times 10^5/T_e)$	19.8
R2	$e + He \longrightarrow He^{**} + e$	$(1.0 \times 10^{-14})\exp(-4.02289 \times 10^5/T_e)$	19.0
R3	$e + He \longrightarrow He^+ + 2e$	$(7.0 \times 10^{-14})\exp(-5.802253 \times 10^5/T_e)$	24.6

The fits for electron and electron energy mobility for the capacitively coupled He discharge case are as follows:

$$\mu_e = -\exp\big(55.0 + 0.3942\log(\epsilon) + 2.134/(\epsilon)$$
$$-0.6433/(\epsilon)^2 + (0.07112)/(\epsilon)^3\big)/N_{\text{gas}} \quad (A.1)$$

$$\mu_\epsilon = \frac{5}{3}\mu_e. \quad (A.2)$$

The electron and electron energy diffusion coefficients, D_e and D_ε, are obtained from their corresponding mobilities using the Einstein relation. In equation (A.1), ε stands for the mean electron energy in units of eV. Mobility of He$_+$ ions are obtained from the expression provided by Turner *et al* [37]:

$$\mu_{\text{He}^+} = 2.69\Big(1 + 1.2 \times 10^{-3}(E/N)^2 +$$
$$\times\, 4.2 \times 10^{-8}(E/N)^4\Big)^{(-0.125)}. \quad (A.3)$$

The corresponding diffusion coefficient for He$^+$ is obtained using Einstein's relation, $\mu k_{\text{B}}T/Ze$.

It should be noted that there was a typographical error in the expression for the mobility of He$_+$ in Turner *et al* [37]. The left-hand side of equation (A.3) was incorrectly specified as $\mu_{\text{He}^+}N$, which has been corrected to μ_{He^+} in the current work.

The diffusion coefficients used for the meta-stable states, He* and He**, were obtained from Yuan *et al* [49] and are given by:

$$4.116 \times 10^{-4} \times (P_{\text{atm}}/P_g) \quad (A.4)$$

$$2.029 \times 10^{-4} \times (P_{\text{atm}}/P_g). \quad (A.5)$$

The rate coefficient and the electron mobility used in the anode-directed, N_2 streamer verification case presented in section 2.2.2 are as follows:

$$\log_{10}k = -218.244 + (316.770)\xi + (-203.767)\xi^2$$
$$+ (66.912)\xi^3 + (-11.079)\xi^4 + (0.735)\xi^5, \quad (A.6)$$

and a piece-wise fit for the mobility is used:

$$\mu_e = \begin{cases} 0.1811 & \text{for } \xi < 0.3 \\ (1.0 \times 10^{24}/n_0((1063.323) \\ \quad + (-1197.375)\xi + (691.236)\xi^2 \\ \quad + (-164.0486)\xi^3 + (12.995)\xi^4 \\ \quad + (-16.851)\log(\xi) & \text{for } 0.3 < \xi < 3.0 \\ \quad + (-47.511)\sin(\xi) \\ \quad + (226.179)\cos(\xi) \\ \quad (-1322.495)\exp(-\xi)) \\ 0.0188 & \text{for } \xi > 3.0 \end{cases}$$
$$(A.7)$$

In equations (A.6) and (A.7), ξ stands for $\log_{10}(E/N)$. The electron diffusion coefficient was obtained using the Einstein's relation. These fits were obtained using regression, with the data provided in the plots of Dujko *et al* [40].

In this case, the ion drift-diffusion was assumed to be negligible at the timescales of electron drift-diffusion. Thus, mobility and diffusion coefficients for ions were chosen to be 0 for N_2^+ in this case, as is also done in Markosyan *et al* [39].

ORCID iDs

Taaresh Sanjeev Taneja ⓘ https://orcid.org/0000-0002-0233-2039

Hariswaran Sitaraman ⓘ https://orcid.org/0000-0001-5304-1664

Suo Yang ⓘ https://orcid.org/0000-0002-9924-2645

References

[1] Kobayashi H, Hayakawa A, Somarathne K K A and Okafor E C 2019 Science and technology of ammonia combustion *Proc. Combust. Inst.* **37** 109–33

[2] Elbaz A M, Wang S, Guiberti T F and Roberts W L 2022 Review on the recent advances on ammonia combustion from the fundamentals to the applications *Fuel Commun.* **10** 100053

[3] Choe J, Sun W, Ombrello T and Carter C 2021 Plasma assisted ammonia combustion: Simultaneous NO$_x$ reduction and flame enhancement *Combust. Flame* **228** 430–2

[4] Lin Q, Jiang Y, Liu C, Chen L, Zhang W, Ding J and Li J 2022 Controllable no emission and high flame performance of ammonia combustion assisted by non-equilibrium plasma *Fuel* **319** 123818

[5] Kim G T, Park J, Chung S H and Yoo C S 2022 Effects of non-thermal plasma on turbulent premixed flames of ammonia/air in a swirl combustor *Fuel* **323** 124227

[6] Zhong H, Mao X, Liu N, Wang Z, Ombrello T and Ju Y 2023 Understanding non-equilibrium N$_2$O/NOX chemistry in plasma-assisted low-temperature NH3 oxidation *Combust. Flame* **256** 112948

[7] Faingold G and Lefkowitz J K 2021 A numerical investigation of NH3/O2/He ignition limits in a non-thermal plasma *Proc. Combust. Inst.* **38** 6661–9

[8] Taneja T S, Johnson P N and Yang S 2022 Nanosecond pulsed plasma assisted combustion of ammonia-air mixtures: Effects on ignition delays and nox emission *Combust. Flame* **245** 112327

[9] Shahsavari M, Konnov A A, Valera-Medina A and Jangi M 2022 On nanosecond plasma-assisted ammonia combustion: effects of pulse and mixture properties *Combust. Flame* **245** 112368

[10] Faingold G, Kalitzky O and Lefkowitz J K 2022 Plasma reforming for enhanced ammonia-air ignition: a numerical study *Fuel Commun.* **12** 100070

J. Phys. D: Appl. Phys. **58** (2025) 015204

T S Taneja *et al*

[11] Mao X, Zhong H, Liu N, Wang Z and Ju Y 2024 Ignition enhancement and nox formation of NH$_3$/air mixtures by non-equilibrium plasma discharge *Combust. Flame* **259** 113140

[12] Johnson P N, Taneja T S and Yang S 2023 Plasma-based global pathway analysis to understand the chemical kinetics of plasma-assisted combustion and fuel reforming *Combust. Flame* **255** 112927

[13] Johnson P N, Taneja T S and Yang S 2022 Global pathway analysis of plasma assisted ammonia combustion *AIAA Scitech 2022 Forum* p 0977

[14] Shioyoke A, Hayashi J, Murai R, Nakatsuka N and Akamatsu F 2018 Numerical investigation on effects of nonequilibrium plasma on laminar burning velocity of ammonia flame 2018 *Energy Fuels* **32** 3824–32

[15] Taneja T S and Yang S 2021 Numerical modeling of plasma assisted pyrolysis and combustion of ammonia *AIAA Scitech 2021 Forum* p 1972

[16] Lefkowitz J K and Ombrello T 2017 An exploration of inter-pulse coupling in nanosecond pulsed high frequency discharge ignition *Combust. Flame* **180** 136–47

[17] Lefkowitz J K, Hammack S D, Carter C D and Ombrello T M 2021 Elevated oh production from NPHFD and its effect on ignition *Proc. Combust. Inst.* **38** 6671–8

[18] Pancheshnyi S V, Lacoste D A, Bourdon A and Laux C O 2006 Ignition of propane–air mixtures by a repetitively pulsed nanosecond discharge *IEEE Trans. Plasma Sci.* **34** 2478–87

[19] Pilla G, Galley D, Lacoste D A and Lacas F 2006 Veynante D and Laux C O Stabilization of a turbulent premixed flame using a nanosecond repetitively pulsed plasma *IEEE Trans. Plasma Sci.* **34** 2471–7

[20] Blanchard V P, Minesi N, Bechane Y, Fiorina B and Laux C 2022 O Experimental and numerical characterization of a lean premixed flame stabilized by nanosecond discharges *AIAA SCITECH 2022 Forum* 2255

[21] Pai D Z, Lacoste D A and Laux C O 2010 Transitions between corona, glow and spark regimes of nanosecond repetitively pulsed discharges in air at atmospheric pressure *J. Appl. Phys.* **107** 093303

[22] Guerra-Garcia C and Pavan C A 2023 The backward problem in plasma-assisted combustion: experiments of nanosecond pulsed discharges driven by flames *Appl. Energy Combust. Sci.* 100155

[23] Pavan C A and Guerra-Garcia C 2022 Nanosecond pulsed discharge dynamics during passage of a transient laminar flame *Plasma Sources Sci. Technol.* **31** 115016

[24] Tholin F and Bourdon A 2011 Influence of temperature on the glow regime of a discharge in air at atmospheric pressure between two point electrodes *J. Phys. D: Appl. Phys.* **44** 385203

[25] Aleksandrov N and Bazelyan E 1996 Temperature and density effects on the properties of a long positive streamer in air *J. Phys. D: Appl. Phys.* **29** 2873

[26] Nijdam S, Teunissen J and Ebert U 2020 The physics of streamer discharge phenomena *Plasma Sources Sci. Technol.* **29** 103001

[27] Bouwman D, Teunissen J and Ebert U 3D particle simulations of positive air–methane streamers for combustion 2022 *Plasma Sources Sci. Technol.* **31** 045023

[28] Taneja T S, Yang S and Sitaraman H 2024 1D simulation of avalanche to streamer to spark transition of plasma discharge in ammonia-air combustion *AIAA SCITECH 2024 Forum* 2607

[29] Meek J M 1940 theory of spark discharge *Phys. Rev.* **57** 722

[30] Loeb L B and Meek J M 1940 The mechanism of spark discharge in air at atmospheric pressure. I *J. Appl. Phys.* **11** 438–47

[31] Wang X, Patel A, Bane S and Shashurin A 2021 Experimental study of atmospheric pressure single-pulse nanosecond discharge in pin-to-pin configuration *J. Appl. Phys.* **130** 103303

[32] Shukla B, Gururajan V, Eisazadeh-Far K, Windom B, Singleton D, Gundersen M and Egolfopoulos F 2013 Effects of electrode geometry on transient plasma induced ignition *J. Phys. D: Appl. Phys.* **46** 205201

[33] Sitaraman H and Raja L 2011 Gas temperature effects in micrometre-scale dielectric barrier discharges *J. Phys. D: Appl. Phys.* **44** 265201

[34] Sitaraman H and Raja L 2012 Simulation studies of rf excited micro-cavity discharges for micro-propulsion applications *J. Phys. D: Appl. Phys.* **45** 185201

[35] Hagelaar G Brief documentation of bolsig+ version 03/2016 2016 *Laboratoire Plasma et Conversion dEnergie (LAPLACE), Universit Paul Sabatier* vol 118

[36] Sitaraman H and Grout R 2016 Premixed combustion simulations with a self-consistent plasma model for initiation *54th AIAA Aerospace Sciences Meeting* p 2158

[37] Turner M M, Derzsi A, Donko Z, Eremin D, Kelly S J, Lafleur T and Mussenbrock T 2013 Simulation benchmarks for low-pressure plasmas: capacitive discharges *Phys. Plasmas* **20** 013507

[38] Verma A K and Somafoam V A 2021 An openfoam based solver for continuum simulations of low-temperature plasmas *Comput. Phys. Commun.* **263** 107855

[39] Markosyan A, Dujko S and Ebert U 2013 High-order fluid model for streamer discharges: Ii. numerical solution and investigation of planar fronts *J. Phys. D: Appl. Phys.* **46** 475203

[40] Dujko S and Markosyan A 2013 White R and Ebert U High-order fluid model for streamer discharges: I. derivation of model and transport data *J. Phys. D: Appl. Phys.* **46** 475202

[41] Raizer Y P and Allen J E 1991 *Gas Discharge Physics* vol 1 (Springer)

[42] Goodwin D G, Speth R L, Moffat H K and Weber B W 2021 Cantera: An object-oriented software toolkit for chemical kinetics, thermodynamics, and transport processes (available at: www.cantera.org version 2.5.1)

[43] Sun J, Bao Y and Ravelid J 2024 Konnov A A and Ehn A Plasma-assisted NH3/air flame: Simultaneous LIF measurements of O and OH *Combust. Flame* **266** 113529

[44] Capitelli M, Ferreira C M, Gordiets B F and Osipov A I 2013 *Plasma Kinetics in Atmospheric Gases* vol 31 (Springer)

[45] Pelevkin A V and Sharipov A S 2018 Reactions of electronically excited molecular nitrogen with H2 and H2O molecules: theoretical study *J. Phys. D: Appl. Phys.* **51** 184003

[46] Castela M, Fiorina B, Coussement A, Gicquel O, Darabiha N and Laux C 2016 O Modelling the impact of non-equilibrium discharges on reactive mixtures for simulations of plasma-assisted ignition in turbulent flows *Combust. Flame* **166** 133–47

[47] Taneja T S and Yang S 2022 Comparing low-mach and fully-compressible CFD solvers for phenomenological modeling of nanosecond pulsed plasma discharges with and without turbulence *AIAA Scitech 2022 Forum* 0976

[48] Johnson P N, Taneja T S and Yang S 2024 Effects of spatiotemporal plasma power distribution on the modeling of ignition kernel evolution in quiescent and turbulent methane/air mixtures *J. Phys. D: Appl. Phys.* **57** 455201

[49] Yuan X and Raja L L 2003 Computational study of capacitively coupled high-pressure glow discharges in helium *IEEE Trans. Plasma Sci.* **31** 495–503